The Role of Moist Intrusions in Winter Arctic Warming and Sea Ice Decline

CIAN WOODS AND RODRIGO CABALLERO

Department of Meteorology, and Bolin Centre for Climate Research, Stockholm University, Stockholm, Sweden

(Manuscript received 2 November 2015, in final form 29 February 2016)

ABSTRACT

This paper examines the trajectories followed by intense intrusions of moist air into the Arctic polar region during autumn and winter and their impact on local temperature and sea ice concentration. It is found that the vertical structure of the warming associated with moist intrusions is bottom amplified, corresponding to a transition of local conditions from a ''cold clear'' state with a strong inversion to a ''warm opaque'' state with a weaker inversion. In the marginal sea ice zone of the Barents Sea, the passage of an intrusion also causes a retreat of the ice margin, which persists for many days after the intrusion has passed. The authors find that there is a positive trend in the number of intrusion events crossing 70°N during December and January that can explain roughly 45% of the surface air temperature and 30% of the sea ice concentration trends observed in the Barents Sea during the past two decades.

1. Introduction

Observations show that the Arctic has warmed over the past decades at a discernibly faster rate than the global mean (Cohen et al. 2014). This ''polar amplification'' of global warming is also a robust feature of climate model predictions of the response to increased radiative forcing (Pithan and Mauritsen 2014). Polar amplification can result from a range of different mechanisms. The most often cited is surface albedo feedback, originally proposed over a century ago (Arrhenius 1896), whereby increasing temperature leads to ice and snow melt back in the high latitudes leading to enhanced absorption of solar radiation and temperature gain. Observations show that polar amplification is greatest in the late fall and early winter—specifically the months October to January (ONDJ) (Screen and Simmonds 2010a)—when solar radiation is minimal. This can be explained by a cross-seasonal effect where the extra energy stored in the ocean in spring and summer, owing to the surface albedo feedback, is released to the atmosphere in winter (Serreze and Francis 2006; Serreze et al. 2009). This heating of the atmosphere from below can also explain another characteristic feature of polar amplification—that it is ''bottom amplified'' so that temperature increases faster near the surface than aloft (Screen and Simmonds 2010b). In turn, the bottom-amplified structure of the warming is responsible for the positive lapse-rate feedback in the Arctic seen in climate sensitivity studies (Pithan and Mauritsen 2014).

However, climate model experiments in which surface albedo feedback is absent still show polar amplification (Caballero and Langen 2005; Alexeev et al. 2005; Graversen and Wang 2009), implying that other mechanisms are also active. In particular, recent work has drawn attention to the role of downward longwave radiation in warming the Arctic and driving sea ice retreat (Francis and Hunter 2006; Graversen and Wang 2009; Bintanja et al. 2011; Kapsch et al. 2013; D.-S. R. Park et al. 2015; H.-S. Park et al. 2015a,b). The largest trends in winter surface air temperature (defined as the air temperature 2 m above the surface) and sea ice concentration (SIC) are found in the Barents and Kara Seas (Screen and Simmonds 2010a). About half of the trend in this region has been attributed to increasing downward longwave radiation whose proximate cause is an influx of moisture from lower latitudes that renders the Arctic troposphere more radiatively opaque (D.-S. R. Park et al. 2015).

In previous work (Woods et al. 2013) we studied the statistics of moisture fluxes into the Arctic region. We

Denotes Open Access content.

Corresponding author address: Cian Woods, Department of Meteorology, Stockholm University, Svante Arrhenius väg 16C, 106 91 Stockholm, Sweden.
E-mail: cian@misu.su.se

DOI: 10.1175/JCLI-D-15-0773.1

found that a relatively small set of very intense, spatially localized moisture injection events exert a significant control on the interannual variance in Arctic-mean surface air temperature and downward longwave radiation, while the remaining, weaker influx events have essentially no climatic impact, though they account for over 70% of the total moisture input. Furthermore, a case study showed that the injected moist air formed a filamentary intrusion that penetrated deep into the Arctic basin causing large thermodynamic perturbations in its path. Here, we extend this previous work by computing forward Lagrangian trajectories to follow the intrusions poleward from their point of injection. In this way we generate a set of intrusion trajectories, which allows us to examine the impact of a typical intrusion as it arrives at a point in the Arctic basin. We also assess the extent to which the observed trends in surface air temperature and SIC can be explained by trends in the frequency of intrusion events.

We are particularly interested in the relation between intrusions and the "synoptically driven" transitions between cold, radiatively clear and warm, opaque states characteristic of the ice-covered central Arctic in winter (Stramler et al. 2011; Morrison et al. 2011). The cold state features vigorous radiative cooling of the surface and a strong surface-based temperature inversion, while in the warm state the inversion essentially disappears and surface radiative cooling drops to near zero. A trend toward greater frequency of occurrence of the warm state would be seen, in the seasonal mean, as a bottom-amplified warming accompanied by increased downward longwave radiation. This provides an alternative route to bottom amplification of Arctic warming that does not run through upward warming by surface turbulent fluxes.

The study is based mostly on the European Centre for Medium-Range Weather Forecasts interim reanalysis (ERA-Interim) product, which outperforms other reanalysis products in the Arctic (Jakobson et al. 2012). We validate the results by comparing with available direct radiosonde observations. These data are detailed in section 2. The computation of intrusion trajectories and their statistics are described in section 3, while the local thermodynamic impact of intrusions in the central Arctic and in the Barents Sea is explored in sections 4 and 5 respectively. Trends in intrusion frequency are examined in section 6, while section 7 summarizes our conclusions.

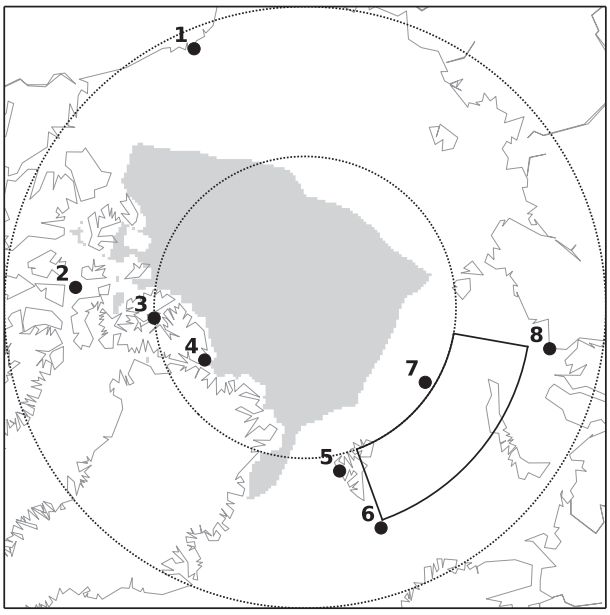

FIG. 1. Region with ONDJ SIC > 90% and trend < 2% decade^{-1} (gray shading). Numbered black dots show the location of the radiosonde stations: 1) Barrow, 2) Resolute, 3) Eureka, 4) Alert, 5) Ny-Ålesund, 6) Bjørnøya (Bear Island), 7) Polargmo (Heiss Island), and 8) Dikson Island. Solid black lines show the Barents Sea box (75°–80°N, 20°–80°E). Dotted lines indicate the 70° and 80°N latitude lines.

2. Data

We use the ERA-Interim dataset (Dee et al. 2011) for the 23 years from 1990 to 2012. Our analysis excludes the 1979–89 decade for two reasons: 1) because polar amplification has been strongest during the more recent decades (Screen and Simmonds 2010b) and 2) for observational consistency—time-varying biases have been reported in the reanalysis owing to the rapid increase in satellite observations beginning in the 1990s (Dee and Uppala 2009). This second point is particularly important for our study, as we focus on attributing and quantifying these trends in the data. The severe paucity of conventional/direct observations in the Arctic during winter implies a high reliance on satellite data in this region. The data are 6 hourly at a resolution of 0.75° and 60 vertical levels. We focus on the late autumn and winter season (ONDJ) since that is when Arctic temperature trends are strongest. We use the convention that the winter of 1990 ends in February 1990.

Radiosonde data for the stations indicated by black dots in Fig. 1 were obtained from the National Oceanic and Atmospheric Administration Earth System Research Laboratory (NOAA ERSL) radiosonde database. Soundings are available every 12 h (excluding missing data) and cover the periods 1990–2012 (stations 1–4) and 1994–2012 (stations 5–8).

3. Moist intrusions

In previous work (Woods et al. 2013) we developed an algorithm to detect intense moisture injection events into the polar region. An injection event is defined as a vertically integrated northward moisture flux across 70°N in excess of 200 Tg day^{-1} deg^{-1} that is sustained for at least

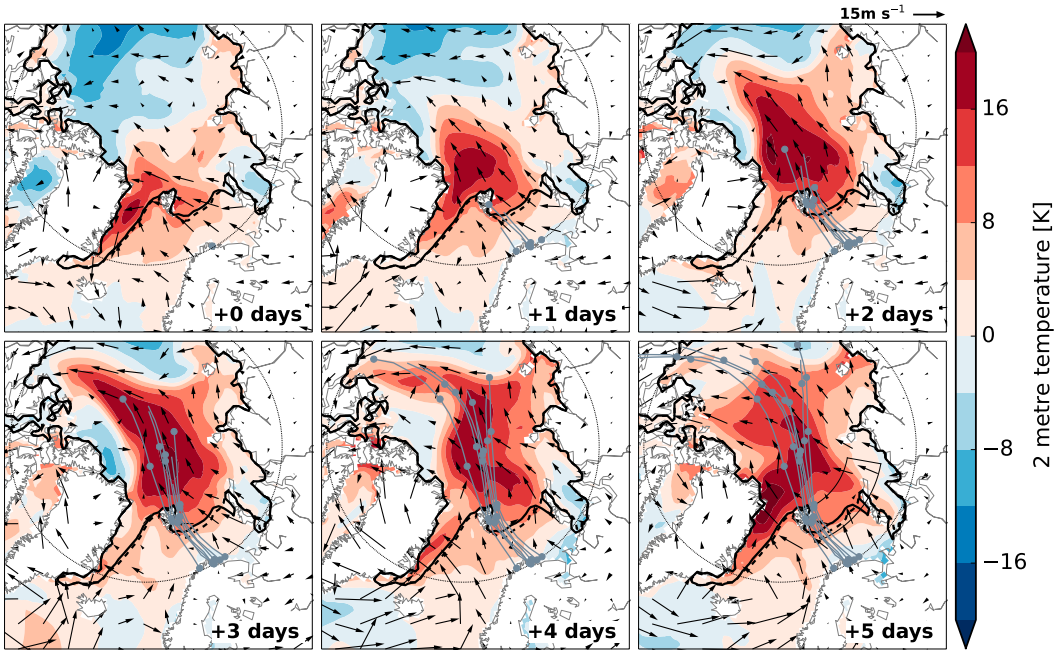

FIG. 2. Case study of an intrusion event beginning over northern Norway at 1800 UTC on 27 December 1999. Each panel shows a snapshot at a time relative to the beginning of the event as indicated in the lower-right corner. Gray lines show centroid trajectories with gray dots at 1-day intervals. Shading shows surface air temperature anomaly from a 6-hourly, smoothed seasonal cycle, arrows show 10-m wind, and the heavy black line shows the 15% SIC contour. As a reference, the dashed black line shows the 15% SIC contour 5 days before the beginning of the event. Dotted line is the 70°N latitude line. Thin black lines in the +5 days panel show the Barents Sea box.

1.5 days and occupies a contiguous zonal extent of at least 9° at all times.

Here, we associate an intrusion event to each injection event by tracking the air injected into the polar region using forward Lagrangian trajectories, obtained by numerically integrating the three-dimensional velocity using a forward Euler scheme:

$$\mathbf{x}(t+\Delta t) = \mathbf{x}(t) + \mathbf{u}(\mathbf{x}, t)\Delta t, \tag{1}$$

where $\mathbf{x}$ and $\mathbf{u}$ are three-dimensional position and velocity, using pressure as a vertical coordinate. Prior to computing the trajectories, we project the three-dimensional wind fields to a Lambert azimuthal equal-area projection, which features a constant gridbox area in km^2 over the domain. This simplifies the trajectory computation, as the distance between grid points on the projection has no latitude dependence. We apply a rotational operation to the horizontal wind components to take account of the fact that, while the projection preserves area, it does not preserve angle. The equation is integrated with a 6-h time step for each of the wind components u, v, and ω. Reanalysis winds interpolated from model levels to 16 standard pressure levels are used; the winds are linearly interpolated at each time step to the instantaneous particle location. An ensemble of 5-day forward trajectories is computed for each injection event; trajectories are initiated at 70°N and 900 hPa at each time step and grid point for which the injection criteria are satisfied over the injection event. The 900-hPa level is chosen because that is where climatological poleward moisture flux across 70°N is maximum (Woods et al. 2013). Given the ensemble of trajectories for each event, centroid trajectories are computed by averaging the concurrent coordinates from all the trajectories initiated at each time step of the event so that each intrusion can be represented by a set of n trajectories, where n is the number of 6-hourly time steps in the injection event. To focus on intrusions that reach deep into the Arctic basin, events in which fewer than 40% of the trajectory ensemble members reaches 80°N over 5 days are discarded. This leaves us with a final dataset of 359 intrusion events from 1990 to 2012, or ~16 per ONDJ season.

An example intrusion event is shown in Fig. 2. The injection occurs over the northern tip of Norway and lasts for 1.75 days, yielding seven centroid trajectories. As the injection event progresses, its centroid shifts slowly eastward, giving some zonal spread in centroid trajectories. The flow field during the event features a large-scale dipole straddling the North Pole, with cyclonic circulation over

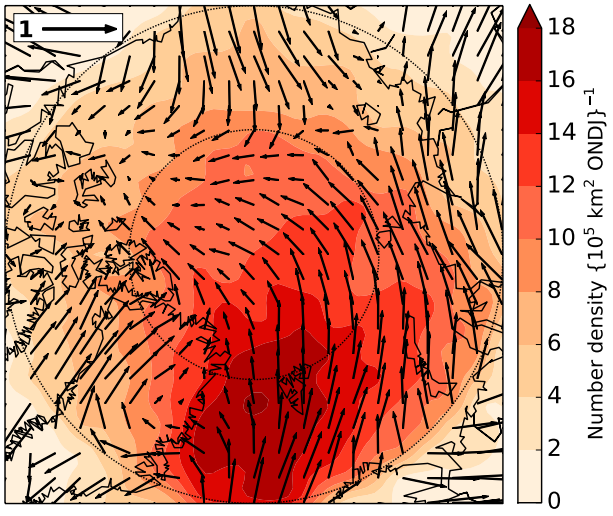

FIG. 3. Climatological intrusion density during ONDJ. Arrows show the mean tangent vector at each point; a value of 1 (shown in upper left) implies all trajectories passing a certain point move in the same direction. Dotted lines indicate the 70° and 80°N latitude lines.

the Atlantic/North American sector and an anticyclone over Eurasia. The trajectories reflect this structure, heading toward the North Pole after injection and then curving cyclonically to exit the Arctic over North America. The intrusion event is associated with large surface air temperature anomalies in the central Arctic and a retreat of the sea ice margin in the Barents Sea, topics we discuss in detail in sections 4 and 5 below.

Figure 3 presents a climatological intrusion density, computed by subdividing the polar region north of 70°N into a 200 km × 200 km grid and counting, for each grid box, the number of intrusions in the dataset with at least one of whose centroid trajectories crosses through the grid box. The arrows in Fig. 3 indicate the typical direction in which intrusions move; this is done by computing a unit tangent vector at each time step along each centroid trajectory and then averaging the tangent vectors within each grid cell. If the trajectories are isotropic the vectors average to zero, while if trajectories have a preferred direction they yield a nonzero mean vector pointing in that direction.

It is clear from Fig. 3 that by far the largest fraction of intrusions enters the Arctic through the Atlantic sector, with smaller numbers entering over the Labrador Sea and Greenland and from the Pacific. Interestingly, intrusions entering via the Atlantic and the Barents/Kara sector typically turn cyclonically toward North America—just as in the case study above—while those entering to the east of the Kara Sea typically turn anticyclonically and exit over Siberia. This suggests that moist intrusions into the Arctic are typically associated with cyclonic anomalies over eastern North America and anticyclonic anomalies over western Siberia, consistent with previous work (Woods et al. 2013; H.-S. Park et al. 2015b).

4. Impact of intrusions in the central Arctic

The case study in Fig. 2 shows that the passage of an intrusion can induce local warming of over 20 K in the central Arctic. Here, we examine the typical thermodynamic impact of intrusions, focusing on the fully ice-covered interior of the Arctic basin—specifically, the region where monthly climatological SIC exceeds 90% and shows negligible trend across the data record. This region is shaded gray in Fig. 1. We compute composites associated with the passage of an intrusion as follows. Each of the centroid trajectories in each intrusion event in the dataset is sampled at 6-hourly time steps beginning from the injection point at 70°N; for each sample point falling within the gray region described above, we select the nearest grid point and extract 9-day time series of vertical temperature and humidity profiles and other fields centered on the time when the trajectory arrives at the grid point. We reduce this total set of events by rejecting those with a surface net longwave flux less than $-30\,\mathrm{W\,m^{-2}}$ on day 0; in this way we focus on the more intense perturbations associated with moist intrusions. We subtract the seasonal mean for the corresponding year and then average over all events.

Results are shown in Fig. 4 (left column). The effects of the intrusion begin to be felt around 3–4 days before arrival of the trajectory centroid; note that the centroid averages over an ensemble of trajectories and will generally lag the intrusion's leading edge. The moisture perturbation (Fig. 4a) is greatest at the inversion level at all times. The temperature perturbation, on the other hand, is initially almost uniform through the troposphere while the surface warms more slowly (Fig. 4c). After about day −1, however, the situation is reversed; the warming is faster near the surface than at the inversion level, and the inversion base moves up off the surface. Surface warming eventually reaches a peak of over 7 K, compared to about 5-K peak warming at the inversion level. Note the slight offset in timing, with peak warming aloft happening around 12 h earlier than at the surface. Note also that the stratosphere shows a slight cooling while the troposphere warms.

After the intrusion centroid passes overhead, tropospheric temperature anomalies decay rapidly while the surface anomaly decays more slowly. This leads to a strong reduction in the mean inversion strength during and after the passage of the intrusion. As shown in Fig. 4e, the surface air temperature perturbation is established very quickly but decays much more slowly, requiring over 10 days (not shown) to relax back to climatological values.

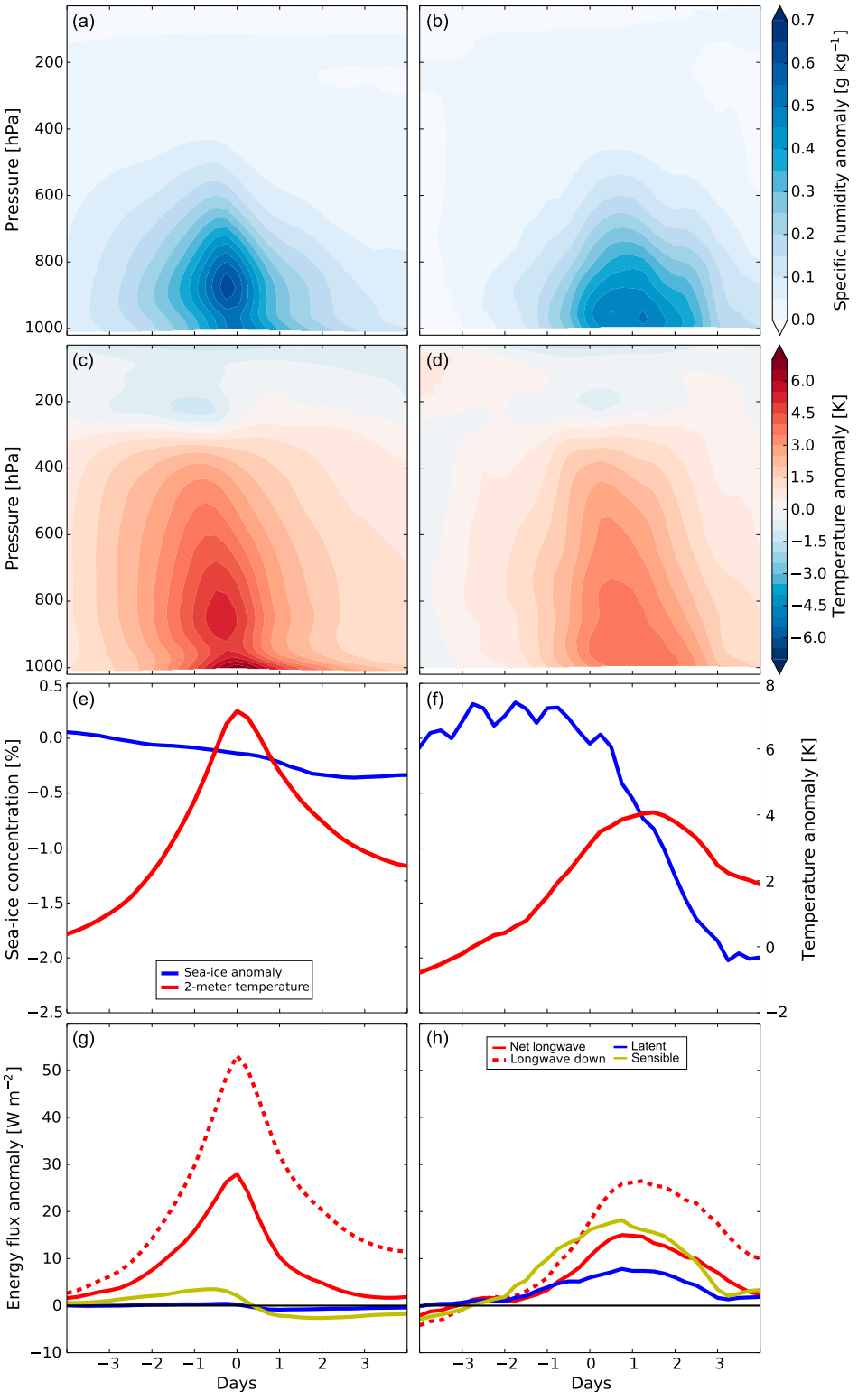

FIG. 4. Composite anomalies showing the thermodynamic perturbation associated with the passage of an intrusion (left) over points in the ice-covered Arctic Ocean during ONDJ and (right) over the Barents Sea box during DJ. (a),(b) Specific humidity, (c),(d) temperature, (e),(f) surface air temperature (red line) and SIC (blue), and (g),(h) surface energy fluxes, defined positive downward. In (g),(h), net longwave radiation is in solid red, downward longwave radiation is in dashed red, sensible heat is in yellow, and latent heat is in blue.

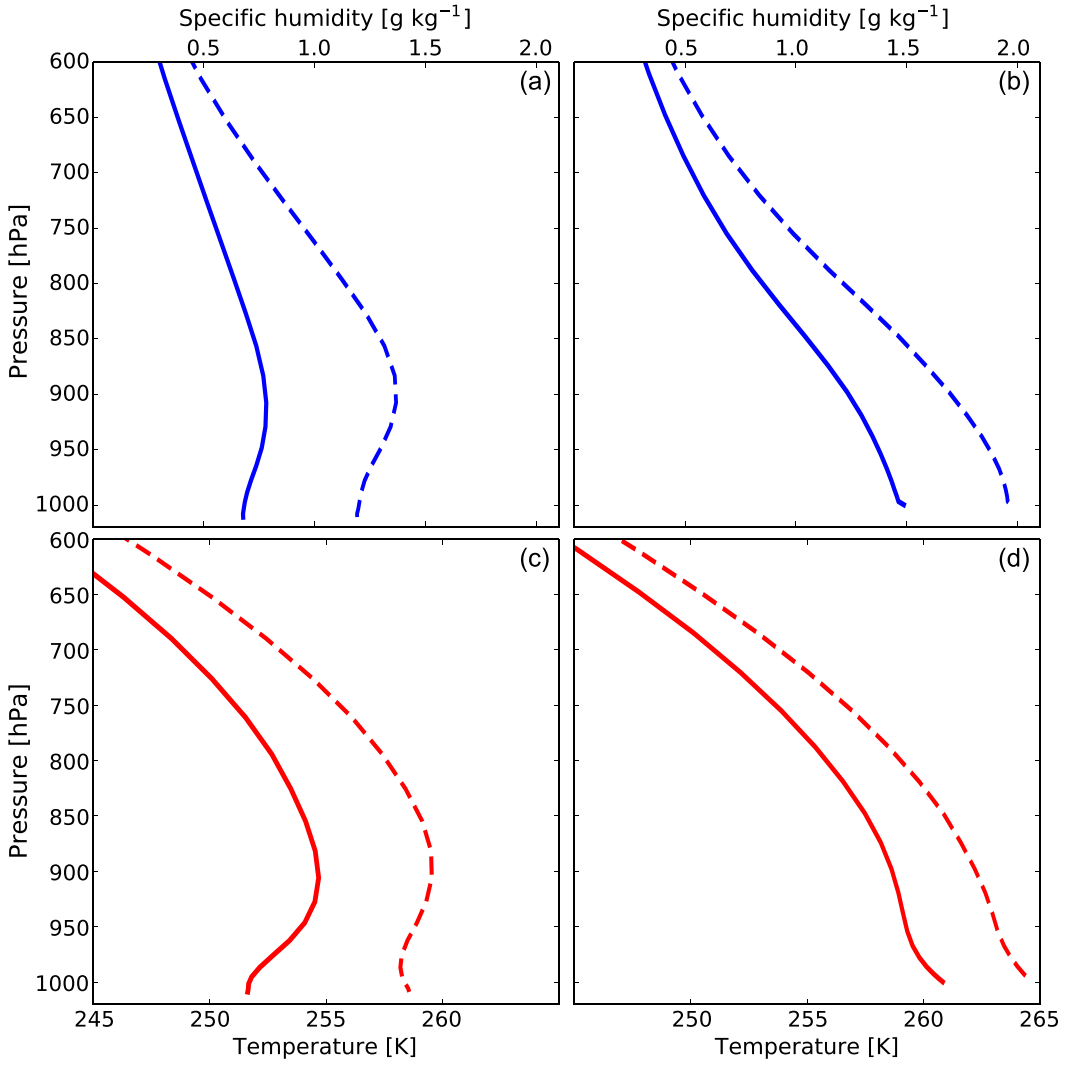

FIG. 5. (top) Humidity and (bottom) temperature profiles (left) in the ice-covered Arctic Ocean during ONDJ and (right) in the Barents Sea box during DJ. Solid lines show climatologies over the respective regions and seasons (representative of typical conditions in the absence of an intrusion event), and dashed lines show profiles at the time of maximum surface warming during a composite intrusion event (representative of conditions at the peak of the event).

Examination of the surface energy budget anomalies (Fig. 4g) shows that surface warming is mostly driven by increased downward longwave flux, owing presumably to radiation from the warm, moist inversion level air, yielding net surface longwave forcing of over 30 W m^{-2}. Sensible heat flux provides a smaller contribution, while latent heat flux is close to zero at all times.

Overall, as shown in Fig. 5, the passage of an intrusion has the effect of bringing local conditions from a near-climatological state with a strong temperature inversion to one with a weak inversion and weak surface radiative cooling. The profiles are remarkably similar to those in the ''radiatively clear'' and ''opaquely cloudy'' states discussed by Stramler et al. (2011, their Fig. 3). Intrusions thus appear as key synoptic-scale drivers of transitions among these states.

One may question the accuracy of the reanalysis in such a data-poor region. We address this question by computing temperature and humidity composites using radiosonde data from stations on the margins of the ice-covered region of the Arctic Ocean, specifically stations 1–4 in Fig. 1. The composites were created by selecting all events in which an intrusion centroid trajectory passed within 200 km of one of the stations and are centered on the time when the trajectory is closest to the station. The results (Figs. 6a,c) show good qualitative agreement with the corresponding reanalysis results (Figs. 4a,c): a bottom-amplified temperature response with a slight time lag between the inversion-level

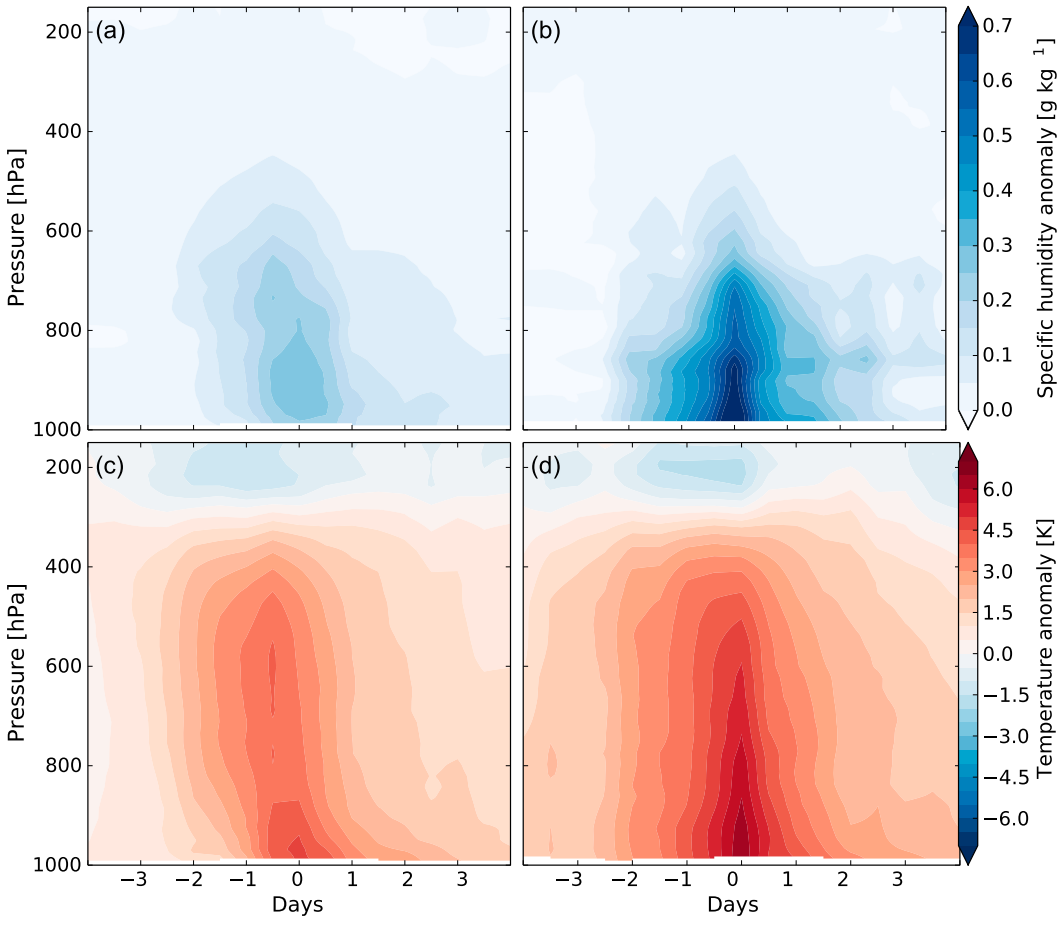

FIG. 6. Observed composite anomalies of (top) specific humidity and (bottom) temperature using radiosonde data from (left) North American high Arctic stations, numbered 1–4 in Fig. 1, during ONDJ and (right) the Barents and Kara Seas, numbered 5–8, during DJ.

and surface peak warming, accompanied by stratospheric cooling, and a humidity response concentrated at the inversion level with smaller values in the boundary layer (contour level not shown). However, it must be noted that the radiosonde data have been assimilated into the reanalysis product, implying that our validation is not entirely independent. We are unaware of any observational datasets that have not been assimilated into ERA-Interim during Arctic winter, meaning a truly independent validation is not possible here. As such, the best validation we can provide is in the most data-poor regions (i.e., the edge of the gray shaded region north of 80°N that faces eastern Siberia). We find that similar composites of specific humidity and temperature in this smaller region exhibit the same qualitative results as described already.

5. Impact of intrusions in the Barents Sea

Here we examine the impacts of intrusions at the sea ice margin, where variability in SIC is largest. We focus on the Barents Sea region, specifically on the box 75°–80°N, 20°–80°E, where observed SIC trends are largest. Our intrusion case study (Fig. 2) shows a substantial retreat of the sea ice edge (identified by the 15% SIC contour) in the Barents Sea following the arrival of the intrusion there.

To assess the average impact of intrusions in this region, we compute composites over all cases in which intrusions pass over the Barents Sea box, centered around the time when the intrusion centroid trajectory first crosses one of the box boundaries. We focus on the period December–January (DJ), when the box is mostly ice covered. Anomalies for each event are computed by subtracting the DJ mean for the corresponding year.

The results are shown in Fig. 7. Surface wind composites indicate that these events are associated with a cyclonic circulation initially centered just west of Svalbard, which drives southerly winds over the sea ice margin in the Barents Sea. The cyclonic circulation then drifts eastward in the first 2–3 days of these events and then

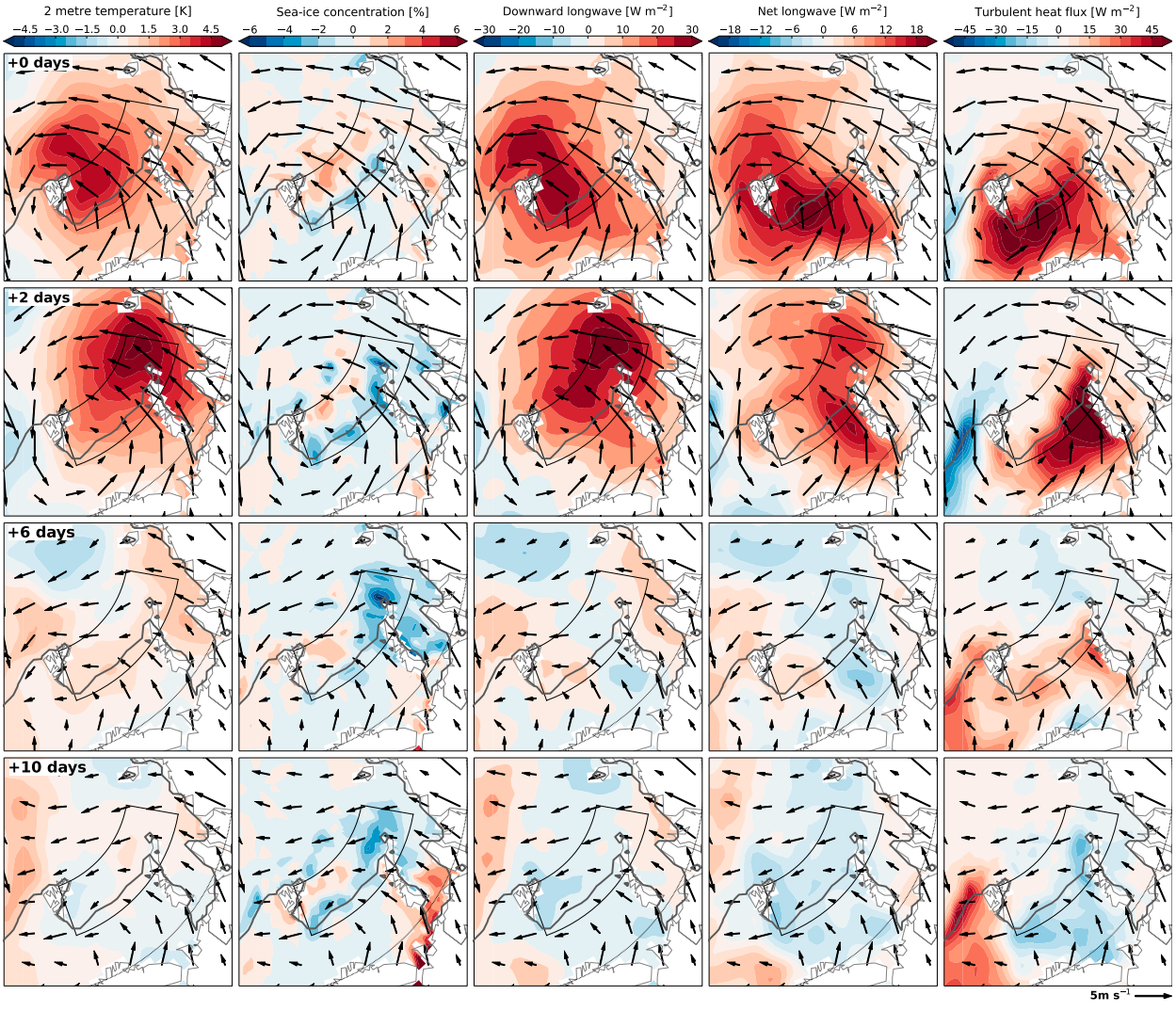

FIG. 7. Composites of (first column) surface air temperature, (second column) SIC, (third column) surface downward longwave radiative flux, (fourth column) surface net longwave radiative flux, and (fifth column) surface turbulent (sensible plus latent) heat flux anomalies over all intrusion events crossing the Barents Sea box (thin black lines in each panel), centered at the time when intrusion trajectory centroids first enter the box. Arrows show composite surface wind. Heavy gray contours show the mean sea ice margin (15% SIC contour) during the composite. Time runs from top to bottom as indicated by the labels in the first column.

southward, resulting in easterly winds over the ice margin after day 6. A surface warming of up to 4.5 K appears first in the west of the box and then propagates eastward in the first few days along with the cyclone; the warm anomaly quickly dissipates after day 6 as easterly winds bring colder air from the Kara Sea. Surface downward longwave flux anomalies largely mirror the evolution of the temperature anomalies, with a positive downward longwave anomaly of up to 30 $W m^{-2}$, which propagates eastward in the first few days and then dissipates. The spatial structure of the anomaly closely resembles that of the surface warming. The surface turbulent (sensible plus latent) heat flux anomaly is also positive in the first few days; the anomaly is very strong (up to 45 $W m^{-2}$) over the open ocean south of the box but much weaker over the sea ice. The surface air temperature response over sea ice is clearly driven mostly by the longwave perturbation.

These thermodynamic anomalies are accompanied by a reduction in SIC of up to 6%. Initially, the negative SIC anomaly is concentrated mostly near the sea ice margin in the south of the box, while a positive SIC anomaly appears in the northern part of the box. This pattern suggests mechanically driven sea ice divergence in the south of the box and compaction in the north. As the event proceeds, however, the negative SIC anomalies expand and by day 6 come to fill most of the box and also

large parts of the Kara Sea east of Novaya Zemlya. It is important to note that although the thermodynamic perturbation has mostly disappeared by day 6, the negative SIC anomalies in the Barents Sea box persist much longer, well beyond day 10. Clearly the processes acting to restore the lost sea ice are slower than those driving sea ice loss at the beginning of the event. As a result, the relatively short-lived intrusion event is followed by a longer period with anomalously reduced sea ice cover. The exposed open ocean—in combination with the shift to easterly winds—yields upward turbulent heat flux anomalies in the latter part of the event, which persist up to and beyond day 20. In the area of the box with reduced SIC, the time-mean effect of the whole event is thus a negative (upward) surface turbulent heat flux anomaly.

Figures 4b,d show box-averaged vertical temperature and humidity profiles composited over the same events. The composites generally resemble those over the central Arctic (Figs. 4a,c) though with considerably weaker amplitude, which is to be expected because of the greater area over which the Barents Sea anomalies are averaged. There are also more subtle differences: the temperature anomaly has a bottom-amplified structure as in the central Arctic but with a more vertically uniform time evolution, and there are humidity anomalies that peak near the surface instead of at the inversion level. Composites of directly observed temperature and humidity in the Barents Sea region during DJ (Figs. 6b,d) show these same features; the amplitude is somewhat higher because these composites are made from individual radiosonde profiles rather than from box area averages as in Figs. 4b,d.

Figure 4f shows that the typical intrusion crossing the Barents Sea box causes a maximum box-averaged surface warming of just under 4 K and a 2% drop in SIC (note that the SIC average includes open-ocean areas with zero SIC and therefore corresponds to an area of ice loss of about $16 \times 10^9\,\mathrm{m}^2$). These anomalies are associated with a positive surface energy budget perturbation (Fig. 4h) peaking at around $35\,\mathrm{W\,m^{-2}}$, to which longwave and sensible heat fluxes contribute about $15\,\mathrm{W\,m^{-2}}$ each while latent heat flux makes a smaller contribution. The question naturally arises as to what extent the SIC perturbation is caused thermodynamically, by melting driven by the surface heating perturbation, or mechanically, by sea ice drift induced by the strong surface winds associated with the intrusion, as mentioned above. This question is difficult to answer in a quantitatively precise way given the paucity of long-term observations of sea ice thickness and drift velocities with adequate spatial resolution. Nonetheless, an order-of-magnitude calculation is useful. If we assume that only net longwave and sensible heat flux contribute to heating the sea ice, Fig. 4h shows an average heating of some $15\,\mathrm{W\,m^{-2}}$ over the first 4 days of the event. This energy is sufficient to melt roughly 1.5 cm of ice, which given a climatological sea ice thickness of around 70 cm averaged over the Barents Sea box (H.-S. Park et al. 2015b) is equivalent to a 2% drop in SIC, comparable to the observed box-mean drop in SIC over the same period (Fig. 4f). This is of course a very crude estimate: on the one hand, it underestimates the potential ice melt since the contribution from upward heat flux through the ice is ignored and the downward longwave flux is almost certainly biased low because of insufficient Arctic cloud opacity in the ERA-Interim product (Engström et al. 2014); on the other hand, it overestimates the actual SIC reduction since not all the energy goes into melting sea ice (some goes into raising the temperature), and even where ice melts, it may simply reduce ice thickness without creating open ocean and reducing SIC. However, it implies that thermodynamic forcing by the intrusion cannot be ruled out as an important driver of sea ice retreat. A more sophisticated estimate (H.-S. Park et al. 2015b) arrives at a similar conclusion.

6. Trends

We now turn to the question of whether the Arctic warming and sea ice decline observed in the past decades can be explained by a rising frequency of intrusions. As shown in Fig. 8a, the number of moisture injections into the Arctic region during December and January has approximately doubled since 1990, while October–November counts have increased by 13% and are statistically insignificant over the same period. We note that the trends in DJ as well as being statistically significant are also robust to the choice of flux threshold, showing an average increase of 80% since 1990 when the threshold varies in the range 200–300 $\mathrm{Tg\,day^{-1}\,deg^{-1}}$. We therefore focus only on DJ in what follows.

Injection events are a combined function of both meridional velocity v and specific humidity q. A natural question arises whether the positive trend in injection event numbers has been driven by v, q, or both. To address this question, we compute the average v and q within the detected injection events at 70°N and take the difference between the periods 1990–2001 and 2002–12 for each variable. Our results show that there has been an increase in q at all levels between these two periods, while v has remained relatively constant (actually decreasing slightly on average between the two periods). Thus, the positive trend in injection events during DJ has most likely been driven by an increase in q at 70°N.

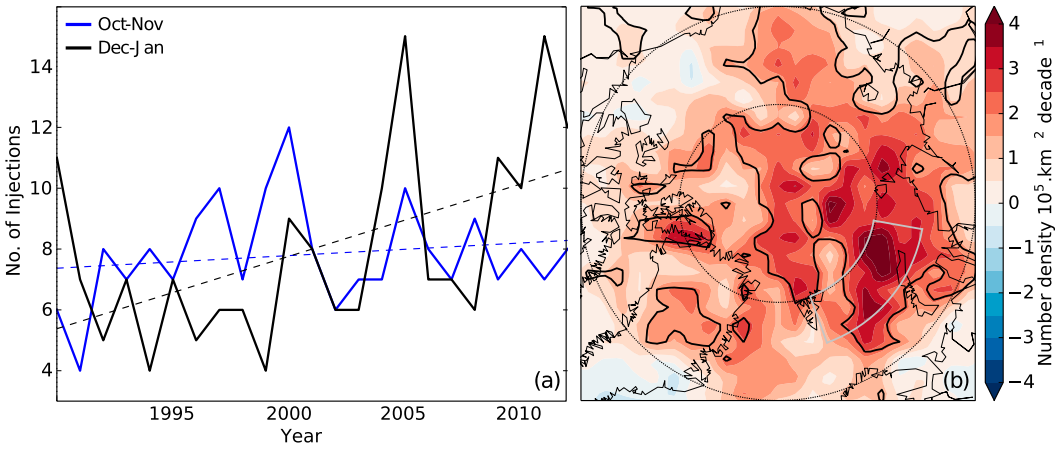

FIG. 8. (a) Total number of intrusion events during October–November (blue line) and December–January (black) for each year in the dataset. Dashed lines show linear fits. There is a significant trend in the number of intrusions during December–January of roughly 2.5 decade^{-1} ($p = 0.005$). (b) Linear trends in intrusion density during December–January. Solid black lines enclose trends significant at the 5% level. Gray lines show the Barents Sea box. Dotted lines show the 70° and 80°N latitude lines.

Figure 8b shows the trend in DJ intrusion density associated with the increasing injection frequency. Statistically significant trends are concentrated over the Barents Sea and central Arctic, with secondary maxima in the Pacific sector and over the Canadian Archipelago.

Given the impacts of individual intrusion events discussed above, we might expect a greater number of intrusions to result in seasonal-mean warming and sea ice loss. These statistically implied trends can be determined by using the interannual variability to estimate the impact of a single intrusion on seasonal-mean temperature and SIC and then multiplying by the trend in intrusion numbers. More precisely, we write

$$N_i = N_0 + \gamma_N i + \Delta N_i,$$

where N_i is the intrusion density at a given grid point (see section 3) for DJ of year i, N_0 is a constant, γ_N is a trend coefficient (with units of intrusions per year), and ΔN_i is a residual reflecting interannual variability around the trend. An analogous decomposition is also applied to the DJ-mean value of surface temperature and SIC at each grid point. We then estimate the impact of a single intrusion on, for example, surface temperature T by regressing interannual fluctuations of intrusion density and surface temperature at the same grid point: $\Delta T_i = a\Delta N_i + b$, where the regression coefficient a has units K per intrusion. Finally, we compute the statistically predicted trend in surface temperature at each grid point simply as $\gamma_T = a\gamma_N$. This method is conceptually similar to that used by D.-S. R. Park et al. (2015).

The regression results (Fig. 9, top row) show a statistically significant impact of intrusions on DJ-mean surface air temperature over the Atlantic and Pacific sectors and over Greenland, where intrusions are relatively close to their injection point, and much weaker impacts over the Beaufort and East Siberian Seas, where they are near the end of their trajectories. Statistically significant SIC response with substantial amplitude is found only in the marginal ice zone of the Barents Sea. Impacts on downward and net longwave fluxes are significant through most of the domain except for a latitude band in the south of the Barents Sea box near the sea ice margin. The turbulent heat flux shows a significant positive response in the open-ocean region of the southern Barents Sea, owing mostly to reduced evaporation, a negative response to the east of Novaya Zemlya.

The statistically predicted trends (Fig. 9, middle row) show a spatial structure that is remarkably consistent—considering the approximations made—with the observed trends (Fig. 9, bottom row). Predicted surface air temperature trends (Fig. 9f) are greatest in the Barents Sea area extending into the central Arctic in agreement with observations (Fig. 9k), with the average trend predicted in the Barents Sea box approximately 45% of that observed. This localization of the trends arises both because intrusion counts have risen most rapidly in that region (Fig. 8b) and because individual intrusions have the greatest impact in that region (Fig. 9a). The predicted trend has a peak amplitude of about 3 K decade^{-1}, about half of the observed value. For SIC the predicted trend (Fig. 9g) again coincides

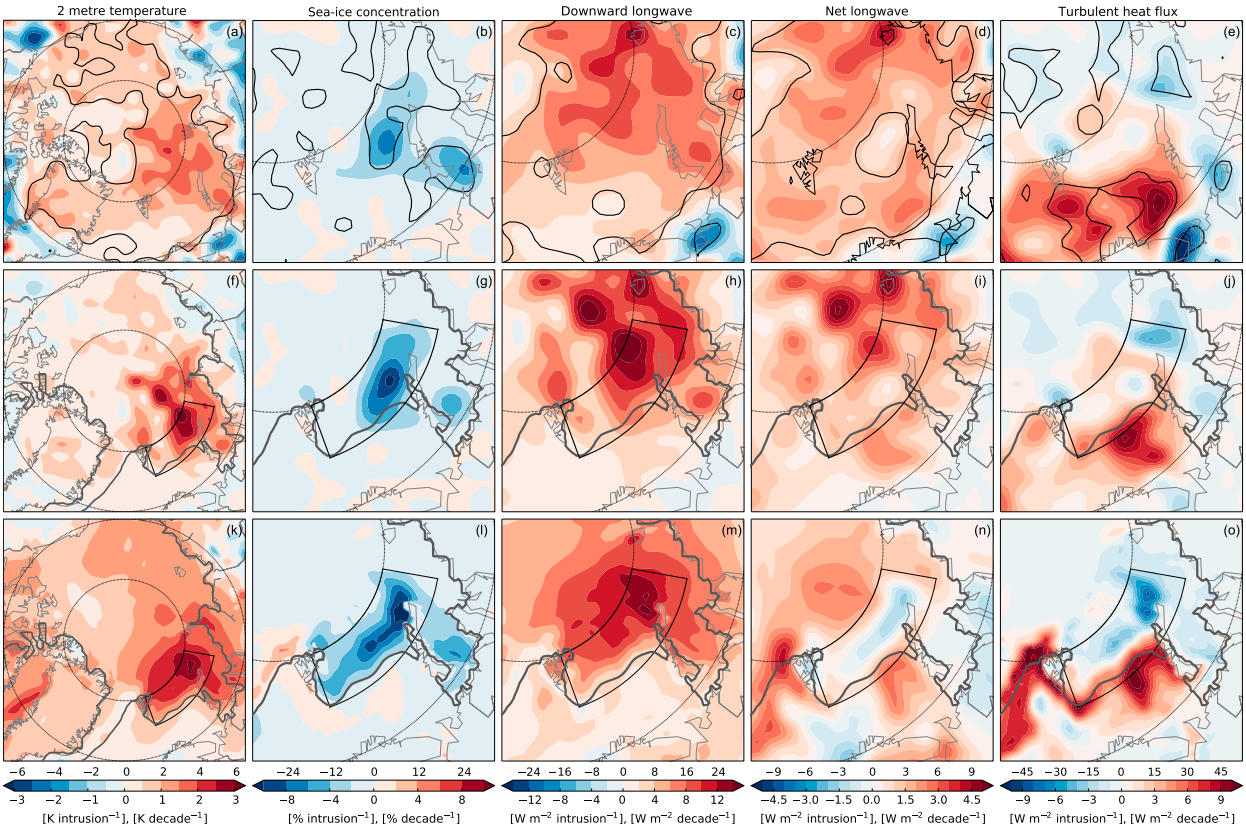

FIG. 9. (Top) Detrended regression of DJ intrusion density at each grid box onto DJ-mean fields; (middle) predicted trend obtained by multiplying the regression field by the intrusion density trends shown in Fig. 8b; and (bottom) observed DJ trends in (first column) surface air temperature, (second column) SIC, (third column) surface downward longwave radiative flux, (fourth column) surface net longwave radiative flux, and (fifth column) turbulent (sensible plus latent) surface heat flux. Heavy black contours in (top) enclose regions where the detrended regression is significant at the 5% level. In (middle) and (bottom), solid black lines show the Barents Sea box and heavy gray contours show the climatological sea ice margin (15% SIC contour). Numbers below the color bars refer to (top) and (middle), and numbers above the color bars refer to (bottom). Dotted lines show the 70° and 80°N latitude lines.

spatially with the observed trend (Fig. 9l) and peaks at about 10% decade^{-1}, or about ⅓ the observed value at the same location, with the average predicted trend in the Barents Sea box being approximately 30% of that observed. As in the composites (section 5), the downward longwave flux trends have a spatial structure almost identical to the surface temperature trend, again implying that the latter is dominated by the former. Observed trends in net longwave flux (Fig. 9n) show slightly negative values in the middle of the Barents Sea box, where SIC trends maximize. This feature is captured by our predicted trend (Fig. 9i), insofar as the local minimum is predicted in the same location as the negative sea ice concentration trends. A similar feature occurs in the observed and predicted turbulent flux trends (Figs. 9j,o) and is in fact also present in the regression (Fig. 9e). As discussed above, these negative trends can be explained by the persistence of sea ice reduction in the aftermath of each intrusion event, which results in surface flux anomalies oriented upward in the time mean.

7. Summary and conclusions

In previous work (Woods et al. 2013) we showed that intense moisture injections across 70°N exert considerable control over the area- and seasonal-mean surface temperature and longwave fluxes in the polar region. Here, we have extended this work in several directions. We have reconstructed the Lagrangian trajectories followed by the intrusions after injection and found that these trajectories are particularly concentrated in the Atlantic sector and curve cyclonically from their point of injection to their typical exit region over North America, taking on the order of 5 days to complete the journey. In their path, the intrusions create strong downward longwave flux anomalies and bottom-amplified temperature perturbations. In the marginal sea ice region of the

Barents Sea, the combined thermodynamical and mechanical forcing associated with the passage of an intrusion causes a retreat of the sea ice margin, which persists much longer than the forcing anomaly itself. We find a significant increase in intrusion density during December and January over the past two decades, and this trend can explain a substantial fraction of the observed trends in surface air temperature, SIC, and other fields. Only a weak positive trend in intrusion numbers is found for October and November, however, so we cannot explain the observed trends in those months using our approach. Other mechanisms must be invoked to explain trends during these late autumn months; processes such as an extended melt season and associated later autumn freeze onset are likely candidates (Markus et al. 2009).

A key feature of the warming trend in the Arctic is that it is bottom amplified (i.e., that it is in fact a trend toward a weakening of the climatological temperature inversion that prevails in ice-covered regions of the Arctic basin in winter). This feature has previously been mostly attributed to increased upward turbulent heat flux due to sea ice loss (Serreze et al. 2009; Screen and Simmonds 2010a,b). Our results suggest a more nuanced view. The passage of an intrusion affects local conditions by inducing a transition from a "cold clear" state with a strong inversion to a "warm opaque" state with a much weaker inversion, in agreement with recent modeling work (Pithan et al. 2014; Cronin and Tziperman 2015). This yields an overall bottom-amplified local temperature perturbation, owing largely to surface heating by increased downwelling longwave radiation. An increase in the frequency of intrusions can therefore drive bottom-amplified warming trend even in the absence of sea ice loss. In addition, the intrusions themselves drive sea ice retreat in the marginal zone and thus promote the upward turbulent fluxes that help produce bottom-amplified warming.

Our results agree with other recent work showing a strong impact of poleward moisture flux on Arctic sea ice variability and trends (D.-S. R. Park et al. 2015; H.-S. Park et al. 2015a,b). Since most of the moisture flux into the Arctic occurs in a small number of extreme events (Woods et al. 2013; Liu and Barnes 2015), it is natural to take an event-based approach as we do here, which allows us to study the structure of the intrusion events and their link to dynamical processes in the Arctic region and at lower latitudes. Further exploration of these links, and in particular the role of teleconnections from the tropics (Lee et al. 2011; Ding et al. 2014; H.-S. Park et al. 2015b), is an important avenue for future work.

Acknowledgments. We thank Gunilla Svensson for useful discussion and three anonymous reviewers whose comments helped improve the text. Work was supported by the Swedish Research Council and the Swedish e-Science Research Centre (SeRC).

REFERENCES

Alexeev, V., P. L. Langen, and J. R. Bates, 2005: Polar amplification of surface warming on an aquaplanet in "ghost forcing" experiments without sea ice feedbacks. *Climate Dyn.*, **24**, 655–666, doi:10.1007/s00382-005-0018-3.

Arrhenius, S., 1896: On the influence of carbonic acid in the air on the temperature of the ground. *Philos. Mag.*, **41**, 237–276, doi:10.1080/14786449608620846.

Bintanja, R., R. Graversen, and W. Hazeleger, 2011: Arctic winter warming amplified by the thermal inversion and consequent low infrared cooling to space. *Nat. Geosci.*, **4**, 758–761, doi:10.1038/ngeo1285.

Caballero, R., and P. Langen, 2005: The dynamic range of poleward energy transport in an atmospheric general circulation model. *Geophys. Res. Lett.*, **32**, L02705, doi:10.1029/2004GL021581.

Cohen, J., and Coauthors, 2014: Recent Arctic amplification and extreme mid-latitude weather. *Nat. Geosci.*, **7**, 627–637, doi:10.1038/ngeo2234.

Cronin, T. W., and E. Tziperman, 2015: Low clouds suppress Arctic air formation and amplify high-latitude continental winter warming. *Proc. Natl. Acad. Sci. USA*, **112**, 11 490–11 495, doi:10.1073/pnas.1510937112.

Dee, D., and S. Uppala, 2009: Variational bias correction of satellite radiance data in the ERA-Interim reanalysis. *Quart. J. Roy. Meteor. Soc.*, **135**, 1830–1841, doi:10.1002/qj.493.

——, and Coauthors, 2011: The ERA-Interim reanalysis: Configuration and performance of the data assimilation system. *Quart. J. Roy. Meteor. Soc.*, **137**, 553–597, doi:10.1002/qj.828.

Ding, Q., J. M. Wallace, D. S. Battisti, E. J. Steig, A. J. Gallant, H.- J. Kim, and L. Geng, 2014: Tropical forcing of the recent rapid Arctic warming in northeastern Canada and Greenland. *Nature*, **509**, 209–212, doi:10.1038/nature13260.

Engström, A., J. Karlsson, and G. Svensson, 2014: The importance of representing mixed-phase clouds for simulating distinctive atmospheric states in the Arctic. *J. Climate*, **27**, 265–272, doi:10.1175/JCLI-D-13-00271.1.

Francis, J. A., and E. Hunter, 2006: New insight into the disappearing Arctic sea ice. *Eos, Trans. Amer. Geophys. Union*, **87**, 509–511, doi:10.1029/2006EO460001.

Graversen, R. G., and M. Wang, 2009: Polar amplification in a coupled climate model with locked albedo. *Climate Dyn.*, **33**, 629–643, doi:10.1007/s00382-009-0535-6.

Jakobson, E., T. Vihma, T. Palo, L. Jakobson, H. Keernik, and J. Jaagus, 2012: Validation of atmospheric reanalyses over the central Arctic Ocean. *Geophys. Res. Lett.*, **39**, L10802, doi:10.1029/2012GL051591.

Kapsch, M.-L., R. G. Graversen, and M. Tjernström, 2013: Springtime atmospheric energy transport and the control of Arctic summer sea-ice extent. *Nat. Climate Change*, **3**, 744–748, doi:10.1038/nclimate1884.

Lee, S., T. Gong, N. Johnson, S. B. Feldstein, and D. Pollard, 2011: On the possible link between tropical convection and the Northern Hemisphere Arctic surface air temperature change between 1958 and 2001. *J. Climate*, **24**, 4350–4367, doi:10.1175/2011JCLI4003.1.

Liu, C., and E. A. Barnes, 2015: Extreme moisture transport into the Arctic linked to Rossby wave breaking. *J. Geophys. Res. Atmos.*, **120**, 3774–3788, doi:10.1002/2014JD022796.

Markus, T., J. C. Stroeve, and J. Miller, 2009: Recent changes in Arctic sea ice melt onset, freezeup, and melt season length. *J. Geophys. Res.*, **114**, C12024, doi:10.1029/2009JC005436.

Morrison, H., G. de Boer, G. Feingold, J. Harrington, M. D. Shupe, and K. Sulia, 2011: Resilience of persistent Arctic mixed-phase clouds. *Nat. Geosci.*, **5**, 11–17, doi:10.1038/ngeo1332.

Park, D.-S. R., S. Lee, and S. B. Feldstein, 2015: Attribution of the recent winter sea ice decline over the Atlantic sector of the Arctic Ocean. *J. Climate*, **28**, 4027–4033, doi:10.1175/JCLI-D-15-0042.1.

Park, H.-S., S. Lee, Y. Kosaka, S.-W. Son, and S.-W. Kim, 2015a: The impact of Arctic winter infrared radiation on early summer sea ice. *J. Climate*, **28**, 6281–6296, doi:10.1175/JCLI-D-14-00773.1.

——, ——, S.-W. Son, S. B. Feldstein, and Y. Kosaka, 2015b: The impact of poleward moisture and sensible heat flux on Arctic winter sea ice variability. *J. Climate*, **28**, 5030–5040, doi:10.1175/JCLI-D-15-0074.1.

Pithan, F., and T. Mauritsen, 2014: Arctic amplification dominated by temperature feedbacks in contemporary climate models. *Nat. Geosci.*, **7**, 181–184, doi:10.1038/ngeo2071.

——, B. Medeiros, and T. Mauritsen, 2014: Mixed-phase clouds cause climate model biases in Arctic wintertime temperature inversions. *Climate Dyn.*, **43**, 289–303, doi:10.1007/s00382-013-1964-9.

Screen, J. A., and I. Simmonds, 2010a: Increasing fall-winter energy loss from the Arctic Ocean and its role in Arctic temperature amplification. *Geophys. Res. Lett.*, **37**, L16707, doi:10.1029/2010GL044136.

——, and ——, 2010b: The central role of diminishing sea ice in recent Arctic temperature amplification. *Nature*, **464**, 1334–1337, doi:10.1038/nature09051.

Serreze, M., and J. A. Francis, 2006: The Arctic amplification debate. *Climatic Change*, **76**, 241–264, doi:10.1007/s10584-005-9017-y.

——, A. Barrett, J. Stroeve, D. Kindig, and M. Holland, 2009: The emergence of surface-based Arctic amplification. *Cryosphere*, **3**, 11–19, doi:10.5194/tc-3-11-2009.

Stramler, K., A. D. Del Genio, and W. B. Rossow, 2011: Synoptically driven Arctic winter states. *J. Climate*, **24**, 1747–1762, doi:10.1175/2010JCLI3817.1.

Woods, C., R. Caballero, and G. Svensson, 2013: Large-scale circulation associated with moisture intrusions into the Arctic during winter. *Geophys. Res. Lett.*, **40**, 4717–4721, doi:10.1002/grl.50912.